The Longyearbyen CO_2 Lab: fluid communication in reservoir and cap-rock

Farhana Huq[1*], P. C. Smalley[3], Pål Tore Mørkved[1,2], Ingar Johansen[1], Viktoriya Yarushina[1], and Harald Johansen[1]

[1]Institute for Energy Technology, Instituttveien 18, NO-2007 Kjeller, Norway

[2]Department of Earth Science, University of Bergen, NO-5020, Bergen, Norway

[3] Department of Earth Science & Engineering, Imperial College, London SW7 2AZ, UK

*Corresponding author: Farhana Huq

e-mail: farhana.huq@ife.no

Abstract:

The Longyearbyen CO_2 Lab of Svalbard, Norway was established to estimate the potential for geological carbon sequestration at Spitsbergen. Several monitoring wells were drilled in and around the planned CO_2 injection site. These revealed a Triassic to Cretaceous stratigraphy consisting of (from top to bottom) a zone of permafrost, the aquifer, the caprock shale, and the upper, middle and lower reservoir. This paper uses two tools to investigate fluid communication within and between these entities: $^{87}Sr/^{86}Sr$ of formation waters extracted from cores using the residual salt analysis (RSA) method, and the $\delta^{13}C$ of gases, principally methane and CO_2, degassed from core samples.

The Sr RSA data reveal that the upper reservoir rocks have very constant formation water $^{87}Sr/^{86}Sr$ (0.7130) in wells several kilometres apart, suggesting good lateral communication on a geological timescale. However, there is a distinct barrier to vertical communication within the middle reservoir, indicated by a step change in $^{87}Sr/^{86}Sr$ (0.7130 to 0.7112), corresponding to thin but presumably laterally extensive (>1.5 km) lagoonal mudrocks. The aquifer, which shows a gradient in $^{87}Sr/^{86}Sr$, is also interpreted to have some degree of vertical internal communication on a geological time scale. The caprock shale shows large-scale (over 350 m) smooth vertical gradient in $^{87}Sr/^{86}Sr$ (0.7200-0.7130). This is indicative of an ongoing mixing process between high- $^{87}Sr/^{86}Sr$ waters within the caprock and lower- $^{87}Sr/^{86}Sr$ waters in the underlying reservoir. Diffusion and flow modelling of the Sr data suggest that at some time in the past, shale fluid transport properties were enhanced by the formation of temporary pressure escape features (fractures or chimneys) during deep burial and uplift, or cycles of glaciation. Nevertheless, the smooth compositional gradient in the caprock indicates that fluid mixing has subsequently taken place

slowly, dominated by diffusion. This interpretation is supported by the gas isotope data, where systematic variations in gas $\delta^{13}C$ (-50‰ to -32‰) values also indicate slow and incomplete diffusional fluid mixing. These are positive indicators for caprock effectiveness during a CO_2 injection project.

Keywords: CO_2 storage, Sr isotope, C isotope, site characterization, fluid flow, caprock, large-scale CCS

1. Introduction

As a mitigation technique to climate change caused by anthropogenic CO_2 emissions, geological storage of captured CO_2 from large point sources (e.g. coal fired power plants, industrial emissions) is identified as a promising option (Holloway, 1997; Bachu and Adams 2003; IPCC, 2005). Possible geological storage sites are depleted oil and gas reservoirs, large sedimentary basins or coal beds (Benson and Cole, 2008). Before injecting CO_2 in a targeted reservoir, certain criteria have to be met in terms of geological conditions (Bachu, 2003), economic feasibility and public acceptance (Schakley et al., 2009; Waldhober et al., 2009). Reservoirs being considered for potential CO_2 storage must have the required capacity, injectivity, and lateral and vertical confinement (Bachu, 2008). Thus, proper site selection and characterization is a prerequisite for successful implementation of every Carbon Capture and Storage (CCS) demonstration project. It is even more important for large-scale (>10 Mt/yr) CCS, where high injection rates could bring significant geomechanical effects, such as induced seismicity and pressure-activated flow paths (Raess et al., 2014; Verdon et al., 2013).

Traditional site characterization techniques may involve geological mapping, well logging, core analyses, and hydraulic well testing that provide information on compartmentalization, porosity, permeability as well as extent, continuity and variability of the different layers present (Doughty et al., 2008). Identifying compartments or barriers is especially important, for two reasons. Firstly, overall CO_2 leakage risk is dependent on the overall performance of the primary and secondary containment of the targeted reservoir (Oldenburg, 2008); in other words, containment requires the presence of barriers to vertical fluid flow. Secondly, more localized flow barriers within the reservoir may help with the optimal placement and management of

injected CO_2. For example, Woods (2015) contains an extensive discussion of the effect of shale baffles on the dispersal of injected buoyant plumes.

Reservoir compartmentalization has been investigated and assessed intensively in the oil and gas industries as it impacts the complexity of an oil or gas development, and the amount of ultimate production that will be achieved from a given type and quantity of wells (Jolley et al., 2010; Fokker et al., 2012; Smalley et al., 1994). Reservoir geochemistry, involving the use of natural chemical and isotope tracers, is frequently used in hydrocarbon reservoir appraisal to identify potential barriers and baffles that may affect fluid communication within the hydrocarbon reservoir during production (e.g., Smalley et al. 1995; Mearns and McBride, 1999; Schoell et al., 1993). These methods are based on the idea that heterogeneities in fluid properties will gradually mix through time, and evidence of a lack of mixing is an indicator of lack of communication. In this study we apply some of these reservoir appraisal methods to the characterization of a potential CCS site.

In this study, Sr and C isotopes were used as natural tracers to investigate the fluid communication at a potential CO_2 storage site in Norway. The Longyearbyen CO_2 Lab, located on Svalbard's main island of Spitzbergen at the northwestern margin of the Barents Sea Shelf, is a "green showcase" project, which aimed to demonstrate the full value chain of power generation, CO_2 capture and storage with a net zero carbon footprint. The storage site, 5 km east from Longyearbyen, was chosen as a test site for CO_2 injection due to its coal-based closed energy system and good infrastructure for research, education and monitoring (Sand et al., 2014). During the project, several wells were drilled to perform injection and fracture monitoring tests in order to identify the storability of potential sandstone layers where CO_2 could be injected (Sand et al., 2014, Braathen et al., 2012). The targeted reservoir is a

sandstone layer of the De Geerdalen formation located at ~700-1000 m depth. A thick shale layer, just above the reservoir, was identified as a potential caprock. Near the surface, a thick permafrost layer provided another potential seal (Braathen et al. 2012). Mechanical laboratory testing (Bohloli et al. 2014) suggested that pre-existing vertical fractures in the reservoir could re-open in some stress regimes; however, the role of fracturing in the caprock was uncertain. One of the conclusions of these studies is that the geological history of the sedimentary basin, especially the fluid communication beneath the potential storage site is important for understanding and predicting the behaviour of reservoir and caprock (Braathen et al., 2012 and Bohloli et al., 2014) during CO_2 injection and storage.

Therefore, the key objective of this study is to assess the local geological conditions for CO_2 storage by constraining the seal stratigraphy above and within the reservoir from subsurface fluid data.

2. Study location

Anell et al. (2014), Ogata et al. (2014), and Braathen et al. (2012) described the local geological setting of the Longyearbyen CO_2 Lab. The stratigraphic succession includes a permafrost layer, which extends from the surface to approximately 120-170 m, a thin upper aquifer (170-200 m), a thick cap rock layer (approximately 200-680 m) and the targeted reservoir section (680-1000 m), divided into lower, middle and upper units. The permafrost layer consists mostly of the Carolinefjellet Formation (Fm), which is a succession of intercalated sand and mud. The cap rock consists of Rurikfjellet Fm shales with minor sandstone underlain by the Agardfjellet Fm, dark laminated shales with local silty layers. At about 400 m depth, there is a decollement fault zone between the Agardfjellet Fm and the Rurikfjellet Fm. The targeted reservoir is mostly in the De Geerdalen Fm which is shallow marine sandstone with some

shale horizons. Well testing by water injection revealed a zone of underpressure at about 870 m depth where the pressure was 40 bar, which is 47 bar below the hydrostatic pressure of 87 bar (Braathen et al., 2012; Wangen et al., 2015).

In total, eight wells (DH1 to DH8) were drilled at two sites during the project period (Braathen et al., 2012; Sand et al., 2014) to collect core material and gas samples at various depths. The first two drilled wells were located on the western shore of Adventfjorden (Fig. 1) and the rest of the wells were drilled 7.5 km to the southeast, in Adventdalen (Braathen et al., 2012). This paper presents gas and fluid data from 5 (DH2, DH4, DH6, DH7A and DH8) out of the 8 wells drilled in the Longyearbyen CO_2 Lab project as shown in Figure 1.

Fig. 1: Positions of wells (left) DH2, DH4, DH6, DH7A and DH8 at the Longyearbyen CO_2 Lab used in this study (modified after Braathen et al., 2012; Sand et al., 2014). On the right, the location of Svalbard, which is about 2000 km North of mainland Norway

Wells DH4, DH6, DH7A and DH8 are within a distance of 200 m of each other, and can be considered to represent the same site; whereas, DH2 is located 7.5 km away from the others.

3. Samples, analytical methods and data treatment

The core materials collected from wells DH2, DH4, DH6, DH7A and DH8 represent the aquifer, the caprock and the targeted reservoir. Sr isotope data ($^{87}Sr/^{86}Sr$) from residual salts extracted from core material were used to investigate fluid communication. Gas composition (C_{1-5}, CO_2) and stable isotope ($\delta^{13}C$) analyses were performed on gas samples extracted from core materials. In addition, mineralogical analysis using X-Ray Diffraction (XRD; BRUKER D8 Advance) was performed on 58 dry core samples of reservoir and caprock from well DH4.

3.1 Strontium residual salt analysis (Sr RSA)

In total, strontium residual salt analysis (Sr RSA) was performed on 105 samples, which were taken from the central part of the drilled cores in order to avoid contamination from mud infiltration during drilling (Mearns and McBride, 1999; Smalley et al., 1995) and immediately placed into marked plastic bags. Each 2-3 cm^3 sample was gently disaggregated in a mortar and 10 ml of de-ionized water was added. After 20 minutes, the water with the dissolved salts was passed through a 0.22 µl filter and transferred to acid-cleaned plastic containers. The length of this pore salt dissolution step was optimized to avoid the dissolution of more slowly reacting detrital and diagenetic minerals. The samples were evaporated and the residues were measured utilizing a Finnigan MAT 261 thermal-ionization mass spectrometer (Munz et al. 2010). Repeated measurements of the SRM 987 standard at the time of analysis yielded an average $^{87}Sr/^{86}Sr$ of 0.710260 with the reference value being 0.710254.

3.2 Gas sampling and analysis

Gas sampling and analysis were performed on 80 core samples from wells DH6 and DH7A. The cores (5-10 cm long) were placed inside custom-made cylindrical polyethylene sample containers closed at both ends with valves, as shown in Fig. 2, immediately after drilling. Each sample container was flushed with helium three times in order to expel trapped air. After that the containers were evacuated to 1-2 mbar and the cores were allowed to degas. A port was connected at one end for gas sampling. The gas was collected at 5, 12, and 26 months after core retrieval for well DH6 and at 7, 16, and 28 months for well DH7A. After the first sampling, the remaining gas in the containers was flushed out with He followed by an evacuation to approximately 1-2 mbar. As before, the cores were then allowed to degas until the next sampling period. After the second gas sampling, any further gas evolution was expected to be minimal, and the previous procedure of flushing and evacuating was not repeated and the remaining part of the desorbed gas, after sampling, was left in the container. However, further gas was evolved, and this means the final gas sampling step contained a gas mixture of previous and newly desorbed gas. Some cores did not yield measurable amounts of gas in the later sampling steps.

Gas compositions (C_1 to C_5 and CO_2) were measured using gas chromatography (GC; Agilent 7890 RGA) and stable isotopes ($\delta^{13}C$) were measured using gas chromatography isotope ratio mass spectrometry (Nu Horizon GC IRMS).

Fig. 2: Drilled cores from the wells on the right and custom-built cylindrical polyethylene containers for core degassing on the left

3.3 Correction of carbon isotopes for fractionation during degassing

During the period of desorption of gas from rock samples, gas carbon isotopes fractionate in a pattern that can be modelled as a Rayleigh distillation phenomenon (Ray & Ramesh, 2000). This means that the measured $\delta^{13}C$ in the evolved gas may not directly reflect the composition of the original bulk gas; rather this has to be calculated from the measured data by correcting for this fractionation process.

To investigate this potential problem, the method described in Appendix A was used to reconstruct the original bulk gas composition in each sample. The corrected methane data and the equivalent raw data for comparison are shown in Appendix A (Table A1 and Figure A3). The corrected value was always close (usually within 2‰) to the first-released gas composition, so the subsequent interpretations simply use the first-evolved gases.

4. Results

4.1 Sr RSA

Strontium isotope data for the sampled wells are presented in Fig. 3 and Table B1 in Appendix B. The merged data provide a complete depth profile starting from the permafrost layer down to the reservoir section. The Sr RSA data show significant and systematic variations.

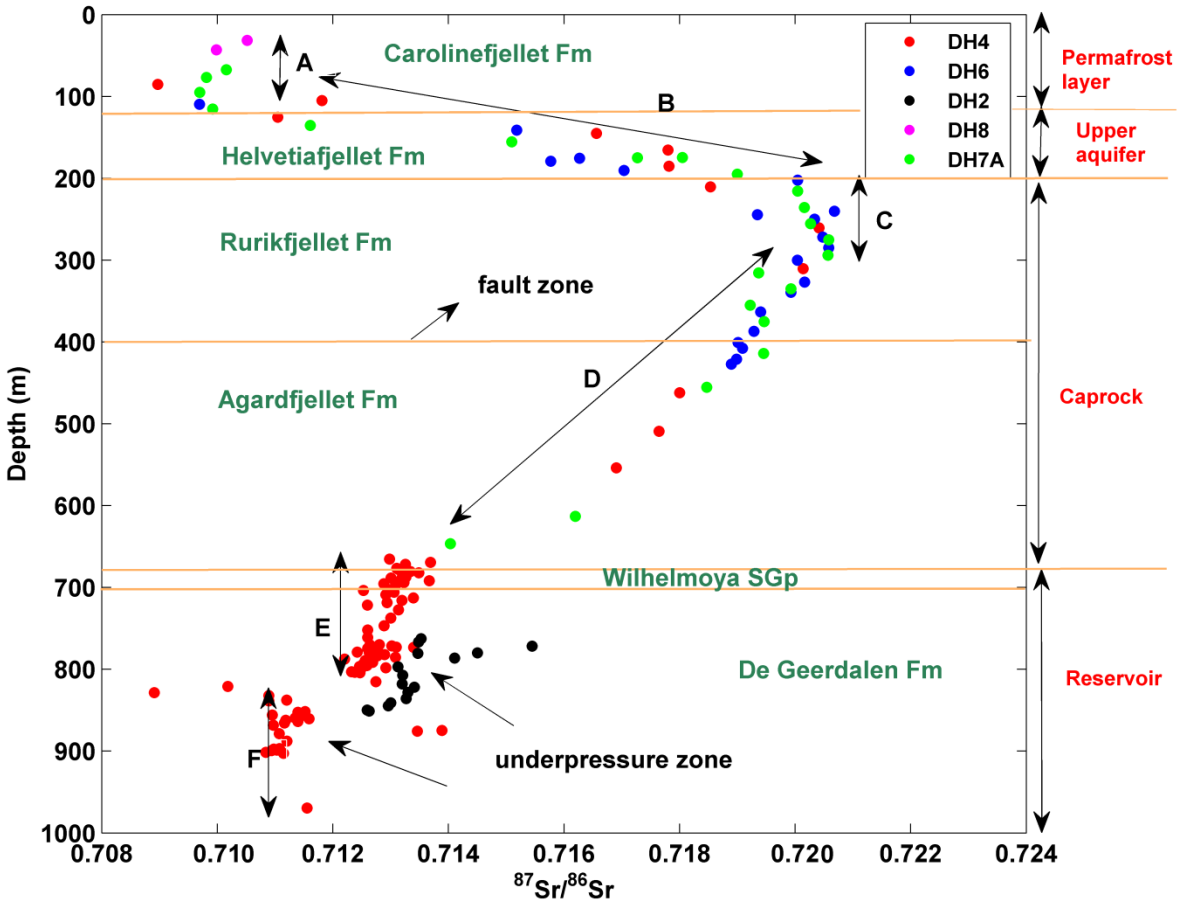

Fig. 3: $^{87}Sr/^{86}Sr$ ratio over depth from residual salt analysis for wells DH2, DH4, DH6, DH7A and DH8. The analytical reproducibility is less than the size of the symbol. Segments A-F are discussed in the text. The reservoir stratigraphy is modified after Braathen et al. (2012). Note that all wells are within 200 m of each other and have similar stratigraphy, apart from well DH2, which is 7.5 km away and where the De Geerdalen Fm is 80 m deeper compared to other wells.

The $^{87}Sr/^{86}Sr$ pattern with depth can be divided into 6 segments (Fig. 3):

A. From surface to ~100 m depth, $^{87}Sr/^{86}Sr$ is constant at ~0.7100. This corresponds to the zone of permafrost and is partly within 5-10 ka glaciomarine deposits (top two samples) and partly within the Cretaceous Carolinefjellet Fm.

B. From 100 m to 200 m depth, $^{87}Sr/^{86}Sr$ increases gradually with depth from ~0.7100 to ~0.7200. Between the samples from depth 135.42 m and 141.25 m, isotopic composition shifts significantly from 0.7116 to 0.7152, but this is interpreted as reflecting a gradient rather than a step. This overall trend is mainly within the Cretaceous Helvetiafjellet Fm (Fig. 3).

C. From 200 m to 300 m depth, $^{87}Sr/^{86}Sr$ is constant at ~0.7200. This segment is completely within the predominantly shaley Rurikfjellet Fm of Cretaceous age (Fig. 3).

D. From 300 m to 650 m depth the $^{87}Sr/^{86}Sr$ ratio decreases gradually from ~0.7200 to 0.7130. This occurs within the predominantly shaley succession in the lower part of the Rurikfjellet Fm and the Jurassic Ågårdfjellet Fm.

E. From 650 m to 820 m $^{87}Sr/^{86}Sr$ is almost constant at 0.7130, with a very slight decrease in $^{87}Sr/^{86}Sr$ with depth. This occurs in the predominantly sandy Triassic rocks of the Wilhelmøya Supergroup and the De Geerdalen Fm. This segment is about 80 m deeper in well DH2, which is 7.5 km away from the drill site of the other wells.

F. From 820 m to 970 m, $^{87}Sr/^{86}Sr$ is almost steady at 0.7112 (2σ =0.000026). This represents the lower part of the Triassic De Geerdalen Fm.

4.2 Gas compositions and isotope analysis

Gas composition data from the first sample degassing step (7 months) in well DH7A are plotted against depth in Figure 4. Gas dryness was also plotted against depth in Fig. 4, where dryness is:

Concentration of methane /∑concentrations of ethane and propane.

Gas samples from the cores of well DH6 were collected after five months of degassing. Well DH6 showed similar results (Fig. A3 in Appendix A).

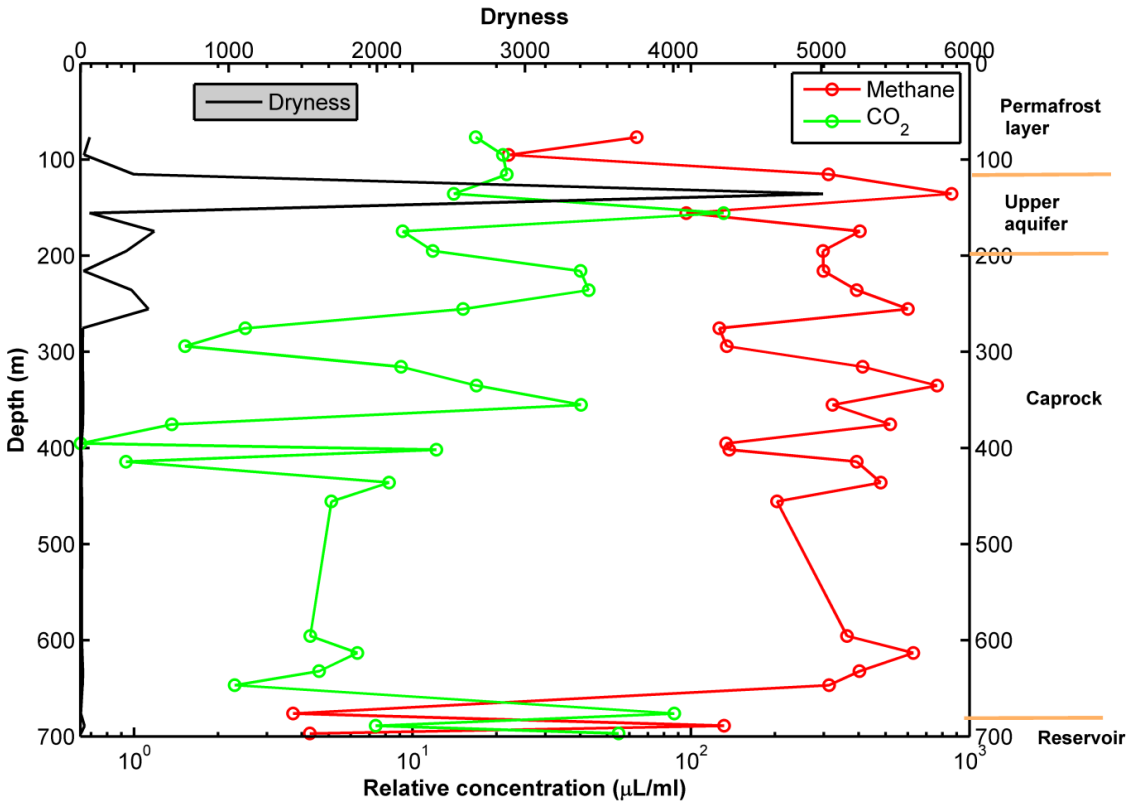

Fig. 4: CO_2 and methane contents, plus gas dryness, over depth after seven months of degassing from cores of well DH7A. Error of measurement is 3% (2σ)

Gas was sampled from 76.8 m in the permafrost down to the bottom of the cap rock layer at 680 m. Only a few samples from the reservoir section (680-700 m) were available as the wells were not drilled any deeper. The major gas present in the cores was methane with minor amounts of ethane, propane and CO_2. In some core samples, butane and ethylene were also observed. In this paper, we focus on the

major components, methane and CO_2. The relative concentration of methane varies between 100 to 850 µL/ml and the maximum relative concentration (850 µL/ml) was observed at about a depth of 135 m (Fig. 4). The CO_2 average relative concentration is an order of magnitude lower than that of methane. The relative concentration of CO_2 varies with depth in a similar pattern to methane, within the range 10-130 µL/ml and with a maximum value at ~155 m depth.

Carbon isotopes of methane and CO_2 from the first degassing step of cores from wells DH6 and DH7A are plotted against depth in Fig. 5. Carbon isotope data for methane degassed at later time steps are presented in Table A1 in Appendix A.

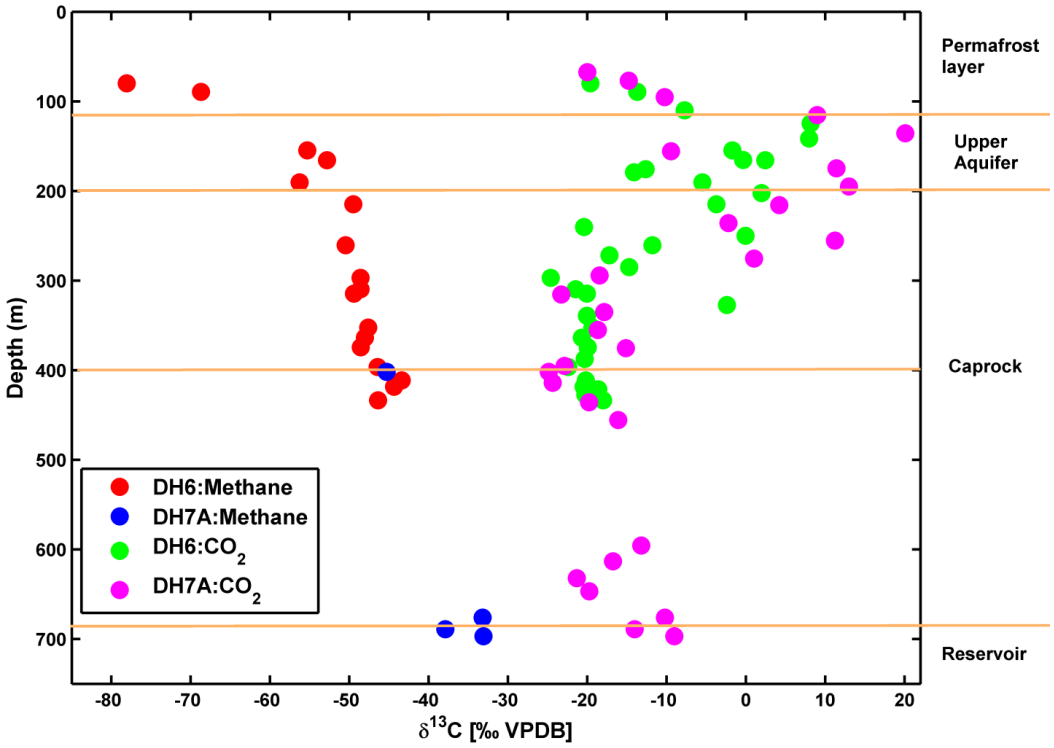

Fig. 5: Carbon isotopes of methane and CO_2 versus depth in gas samples from cores of wells DH6 and DH7A for the first degassing time step. Error of measurement is 0.5‰ VPDB (2σ)

At the permafrost layer (77 to 95 m), $\delta^{13}C_{methane}$ values are low ranging from -72 to -68‰ increasing downwards in the aquifer to -50‰. In the caprock, the $\delta^{13}C_{methane}$

values are constant at just above -50‰ for the upper ~100 m before then starting to increase with depth to about -32 ‰ at the base of the caprock and the uppermost part of the reservoir (Fig. 5).

Except in the upper aquifer, CO_2 carbon isotopes range from -25 to -10‰. In the upper aquifer above 200 m, $\delta^{13}C_{CO2}$ is very high and approaches +20‰.

4.3 XRD analysis

XRD analysis was performed on samples from selected depths in well DH4 and then the mineralogy was reconstructed as presented in Fig. 6.

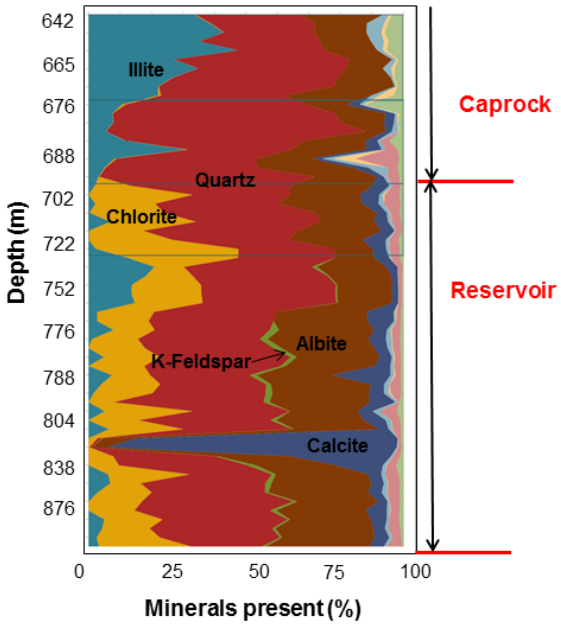

Fig. 6: XRD analysis of the reservoir rock section from the well DH4. Error of measurement is ±3%.

The reservoir rock mostly consists of quartz, albite and clays (illite and chlorite). Minor K-feldspar was observed below 752 m. Calcite cement was evident from 676 m down to the bottom of the reservoir. A thin heavily calcite-cemented layer was detected at about 836 m.

5. Discussions

5.1 Sr RSA

5.1.1 Formation water $^{87}Sr/^{86}Sr$ values

The consistency of the $^{87}Sr/^{86}Sr$ data within and between wells suggests that the data quality has not been significantly affected by contamination of Sr from drilling fluid, which would have led to much more erratic local variations rather than smooth patterns with depths (see examples in Smalley et al., 1995; Mearns and McBride, 1999). This indicates that the Sr RSA data are a reliable measure of the actual pore water $^{87}Sr/^{86}Sr$.

The $^{87}Sr/^{86}Sr$ of the formation waters varies between approximately 0.709 and 0.721, much higher than seawater $^{87}Sr/^{86}Sr$ during the deposition of these sediments (0.7069-0.7079, Smalley et al., 1994). It is thus likely that the formation water $^{87}Sr/^{86}Sr$ is heavily influenced by post-depositional water-rock interaction involving K-bearing silicate minerals. K-rich minerals such as muscovite, mica or K-feldspars have very high Rb/Sr ratios and thus accumulate high $^{87}Sr/^{86}Sr$ through time. For example, K-feldspars studied by Siebel et al. (2005) had $^{87}Rb/^{86}Sr$ ratios >1 and developed $^{87}Sr/^{86}Sr$ >>0.72 after only tens of millions of years. Muscovite studied by Eberlei et al. (2015) had $^{87}Rb/^{86}Sr$ ratios exceeding 1000 and $^{87}Sr/^{86}Sr$ >5. In the Svalbard samples, K-feldspar is common, and is sufficiently abundant (>5%) to be detected by XRD in the lower part of the reservoir section (Fig. 6). Petrographic studies show that the feldspar has textures indicating partial dissolution. Dissolution of very small amounts (fractions of a percent) of such minerals would lead to formation waters with higher $^{87}Sr/^{86}Sr$ than the original seawater in which the sediments were deposited, in the range observed in the sampled waters. Greater

degrees of dissolution of K-feldspar or micas in the caprock shale in segment C (Fig. 3) could explain its high $^{87}Sr/^{86}Sr$ values (0.72).

Although water-rock interaction explains the overall range of $^{87}Sr/^{86}Sr$ values, it is extremely unlikely that in-situ *local* dissolution of Rb-rich minerals could account for the detailed patterns, for example the constant water $^{87}Sr/^{86}Sr$ values (segments E,F) and smooth $^{87}Sr/^{86}Sr$ gradients (segments B, D) (Fig. 3). Local water-rock interaction would have led to local (sub-metre scale) variations in water $^{87}Sr/^{86}Sr$ due to the type, Rb/Sr ratio and age of the detrital minerals in each specific location, and the resulting $^{87}Sr/^{86}Sr$ distribution pattern with depth would be expected to be jagged. If any such local variations did arise in the past, they must have subsequently been smoothed by the fluid mixing processes discussed later.

Two outlying data points at about 834 m, with lower $^{87}Sr/^{86}Sr$, may be influenced by recent (as yet unsmoothed by mixing) dissolution of a calcite-rich layer identified from the XRD analysis (Fig. 6). To support this, $^{87}Sr/^{86}Sr$ of calcite in that depth was measured (See Appendix B, Table- B2) and values were found in the range of 0.7083-0.7095, which is close to the observed formation water data points (0.7089-0.7109).

The overall pattern of $^{87}Sr/^{86}Sr$ variation with depth in segments B, C and D (Fig. 3), with values of ~0.72 in segment C, decreasing smoothly upwards and downwards in segments B and D, is indicative of large scale non-steady-state mixing. In this interpretation, segment B represents mixing between waters with $^{87}Sr/^{86}Sr$ values of ~0.72 in segment C and ~0.71 in segment A, while segment D represents mixing of waters between segments C and E ($^{87}Sr/^{86}Sr$ = ~0.713). It is not possible to construct accurate mixing lines as the formation water Sr concentrations were not able to be measured from the residual salts.

We interpret segment C, with a high $^{87}Sr/^{86}Sr$ value of ~0.7200, as the surviving remnant of high $^{87}Sr/^{86}Sr$ values that may have been present throughout the caprock shale at some time in the past. Subsequently, influx of water with a $^{87}Sr/^{86}Sr$ value of ~0.7100 occurred in segment E, and segment D represents the gradual mixing of these two water end members. Later, water influx in segment A and the upper part of the aquifer in segment B ($^{87}Sr/^{86}Sr$ =~0.7130) set up a mixing system between this water and the caprock shale water in segment C. If this incomplete mixing process went to completion, the resulting steady state $^{87}Sr/^{86}Sr$ pattern with depth (assuming constant Sr concentration) would be a straight line from a value of ~0.7130 in segment A to ~0.7100 in segment E, with the transient high $^{87}Sr/^{86}Sr$ values in the caprock having been completely removed. The questions of exactly which mixing processes were involved and over what timescales are addressed by diffusion and flow modelling in the following section.

5.1.2 Formation water $^{87}Sr/^{86}Sr$ gradients

a) Diffusion mixing models

One possible explanation for the Sr isotope compositional water gradients in segments B and D is that they are the product of diffusional mixing that has not yet reached steady state, which would be characterised by constant values or linear gradients as described above. Analytical models for diffusional mixing of formation waters in general, and Sr isotopes in particular, can be used to place constraints on the mixing processes that are operating (Go et al., 2014, 2012; Smalley et al., 2004). Both segments B and D (Fig. 3) are simple curvilinear trends, indicating that only two mixing end-members are present in each case.

Details of the analytical modelling used here are presented in Appendix B. The modelling results are presented in Fig. 7.

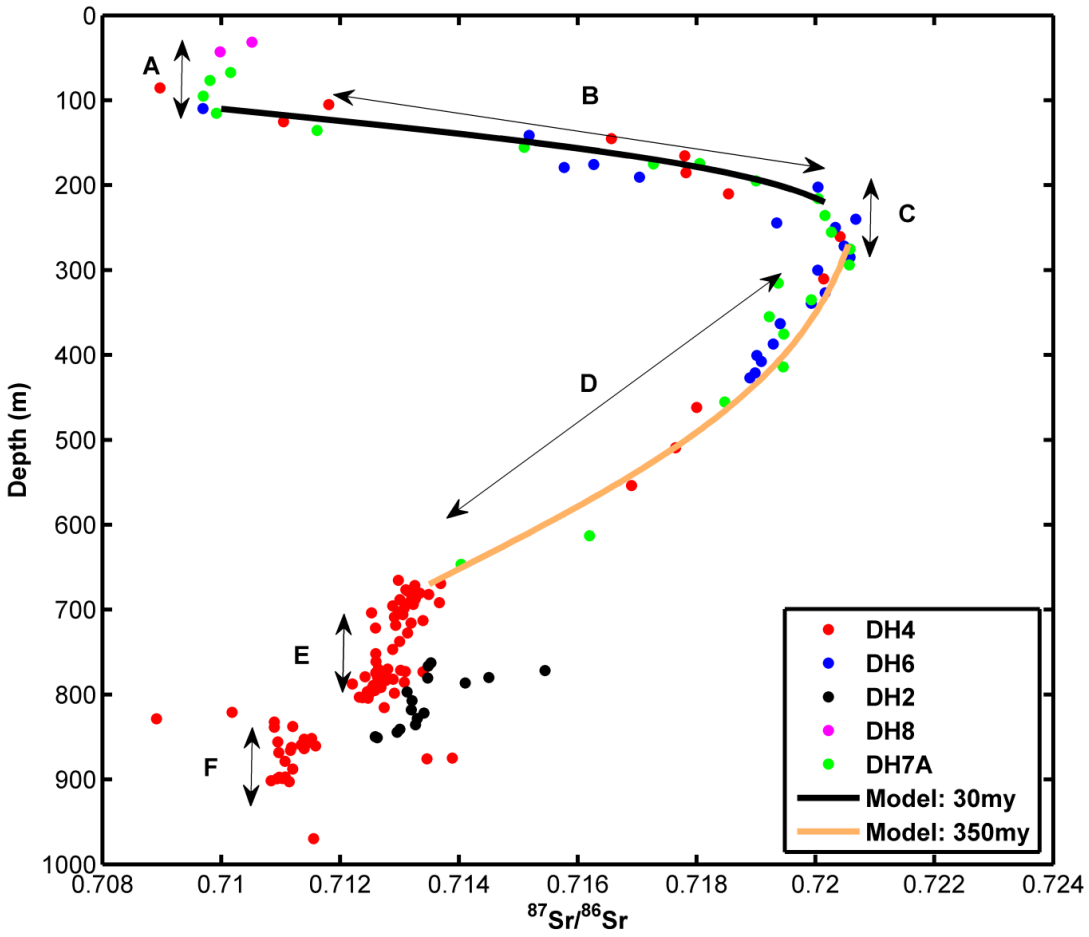

374

375 **Fig. 7:** Diffusional mixing models fitted to the Sr RSA data. See text and Appendix B
376 for model details and explanation

377 **Segment D**: The modelling results indicate that the shape of the $^{87}Sr/^{86}Sr$ gradient
378 (Fig. 7) in segment D is probably a mixture of Sr derived from segments C and E,
379 where segment E is vastly dominant in size and acts as a fixed end member. The Sr
380 RSA data for segment E are indistinguishable in the stratigraphically equivalent
381 samples in wells DH2 and DH4 (Fig. 3), despite these being 7.5 km apart. This
382 indicates that the sands in the upper part of the De Geerdalen Fm could indeed be a
383 large regional reservoir of water with a constant $^{87}Sr/^{86}Sr$ composition.

384 The lateral homogeneity of the segment E water over such a distance cannot,
385 however, be due to diffusional mixing, as this would take longer than the age of the

386 sediments. Rather, the homogeneous composition of the segment E waters must be
387 related to efficient mixing due to fluid flow at some time in the past.

388 The diffusion models described in Appendix B generate mixing curves that closely
389 match the shape of the observed data trends with depth (Fig. 7), which supports the
390 mixing origin of the $^{87}Sr/^{86}Sr$ gradient in segment D. However, the models also
391 demonstrate that diffusion alone cannot account for this mixing, if the assumptions of
392 shale diffusion properties (tortuosity and retardation) are correct. The diffusion model
393 was run to generate the expected $^{87}Sr/^{86}Sr$ gradient over various timescales. Only
394 when the mixing time approached 350 my, did the model results begin to achieve a
395 good visual fit to the shape of the pattern in the Sr data (Fig. 7). As this is longer than
396 the rocks have existed, this is clearly impossible. Thus, there must be an additional
397 mechanism accelerating the mixing process. Candidates include pressure driven flow
398 and modification of shale properties related to the complex loading and unloading
399 history these rocks have experienced. These will be discussed in subsequent
400 sections.

401 The zone of shale fracturing at ~400 m depth (shown on Fig. 3) does not appear to
402 have inhibited the movement of Sr, as it has no influence on the $^{87}Sr/^{86}Sr$ gradient.
403 Thus, there is no indication from the current data that this structural feature either
404 forms a barrier to fluid/ solute movement or provides a pathway.

405 **Segment B**: The $^{87}Sr/^{86}Sr$ gradient in segment B (Fig. 7) can be understood in a
406 similar manner. Diffusional mixing models show that a good fit is achieved from a
407 model where the rocks above ~120 m depth of the Carolinefjellet Fm (segment A)
408 has a fixed composition, Segment C in the upper part of the caprock shale is the
409 other (variable) mixing end member, and segment B is a mixing zone between them.
410 Note that models in which segment C has a fixed $^{87}Sr/^{86}Sr$ have the wrong sense

411 curve (concave upwards) and do not fit the data well. The curve shape matches that
412 of the Sr data using a diffusional mixing time of 30 my. It is possible that the segment
413 B gradient could have been caused by diffusion alone acting over 30 my, but it is
414 equally likely that the mixing has again been enhanced by pressure driven water
415 movement or transient enhancement of shale transport properties as discussed
416 below.

417 The overall pattern of $^{87}Sr/^{86}Sr$ variation through segments A-E can thus be
418 envisioned as two large and homogeneous reservoirs of Sr with relatively low
419 $^{87}Sr/^{86}Sr$ (segments A and E on Fig. 3), with a gradually diminishing high $^{87}Sr/^{86}Sr$
420 signal in segment C (Fig. 7) that is decreasing through mixing from above and below
421 via the mixing zones in segments B and D. This pattern is similar to that seen with
422 natural tracer profiles through other thick shales with adjacent aquifer systems, where
423 mixing is occurring but has not yet reached equilibrium (Mazurek et al., 2011).

424 b) Pressure assisted flow modelling

425 Diffusional mixing on its own would have taken too long to generate the segment D
426 mixing relation between segments C and E, unless aided by other factors such as
427 pressure-driven flow and/or modification of shale properties. Here we examine how
428 pressure-driven flow could have influenced the mixing.

429 The time scale for Darcy flow between segments C and E can be calculated using
430 Darcy's law:

$$v_D = \frac{k_{avg}}{\mu}\frac{\Delta P}{\Delta z}$$

431 Where, v_D is the Darcy flow velocity in ms^{-1}; k_{avg} is the average permeability of
432 segment C to E in m^2; μ is the dynamic viscosity of water ($1x10^{-3}$ Pa s); ΔP is the

pressure difference between the two segments in Pa; Δz is the ~500 m vertical distance between the underpressured (~800 m) and overpressured zone (300 m). Considering typical permeabilities of analogous North Sea shales to be 10^{-19} m^2 (Harrington et al., 2009) and the permeability of the De Geerdalen reservoir to be 10^{-18} m^2 (Magnabosco et al., 2014; Wangen et al., 2015), the average permeability k_{avg} is assumed to be $1.5x10^{-19}$ m^2.

The hydrostatic pressure from overburden at 300 m would be ρgh =$2.94x10^6$ Pa where ρ is the fluid density, g is the gravitational acceleration and h is the depth of interest (300 m here). Assuming a 10% overpressure relative to hydrostatic pressure, P_2, in the shale would be $3.2x10^6$ Pa. Pressure in the underpressured zone in the reservoir at ~800 m is P_1 = 40 bar = $4x10^6$ Pa (Braathen et al., 2012). Substituting these values in the above equation: v_D = $2.4x10^{-13}$ ms^{-1}, With an average porosity between the segments of 0.1, the flow velocity, v, is calculated as $2.4x10^{-14}$ ms^{-1}. Using the flow velocity, travel time for fluid flow can be calculated as:

$t = \Delta z / v$ = $500/2.4x10^{-14}$ = $2x10^{16}$ s = ~600 my

This is an extremely long travel time. Even stretching the assumptions of average shale permeability to higher values does not decrease the pressure-driven mixing timescale to the extent that it could, on its own, generate the observed compositional trends in less than the age of the rocks (Upper Triassic to Middle Jurassic=237 my-163 my).

5.1.3 Interpretation of caprock shale transport properties

The segment D (Fig. 7) mixing gradient cannot be explained by pure diffusion or pure pressure-driven flow mechanisms on their own with typical shale flow and diffusion properties, as the mixing timescale for this would be clearly too long, longer than the

age of the rocks. This points to some kind of enhancement in the shale diffusion and/or flow properties. Possible explanations are discussed below:

a. Average diffusivity was under-estimated. The mixing timescales for diffusion and flow-based processes vary linearly with the assumed diffusivity and permeability respectively. A reasonable mixing timescale would be the time elapsed since the event/process that led to the initial isotopic heterogeneities. For Sr, a reasonable estimate would be the time of maximum burial when the rocks could have experienced the maximum amount of pressure-related mineral dissolution or temperature-related reactions that could have added ^{87}Sr to the formation water. Maximum burial took place at about 36 my ago (Braathen et al., 2012; Wangen et al., 2015; Bohloli et al., 2014). If this time was assumed as a "reasonable geological time frame" then diffusivity would need to be increased by a factor of ~10 to create the segment D gradient by diffusion alone. Although the precise diffusion properties of the caprock shale are uncertain, the assumptions used in the modelling work (Appendix B) were, if anything, on the generous side. It is unlikely that the observed mixing relation could be caused simply by increasing the average diffusivity of the shale.
b. Average permeability was under-estimated. For fluid mixing to occur in the caprock shale over the timescale of 36 my, average permeability would need to be increased by a factor of 18 over that used in the modelling ($1.5x10^{-19}$ m^2). This is unlikely if the lithology of the caprock has been correctly interpreted, as the permeability used is, if anything, on the high side for consolidated shales.

c. Transient increase in diffusivity and/or permeability. In this interpretation, the average diffusion and flow properties of the shale may be correct, but there has been a temporary enhancement of these properties at some time in the past. There are two potential mechanisms for this type of transient event: fracturing during structural deformation, and the formation of temporary localized vertical fluid flow chimneys due to pressure fluctuations. There is some evidence of fracturing generated during early Cenozoic structuration (Braathen et al., 2012) that could have temporarily enhanced vertical fluid flow through the shale before the fractures then closed. There is also evidence in Western Svalbard for the widespread occurrence of active and relict focused fluid flow chimneys or pipes, clearly visible on seismic data (Roy et al., 2014; Bunz et al., 2012; Plaza-Faverola et al., 2011). These are thought to have formed during the repeated glaciation/deglaciation and loading/unloading cycles that have affected the studied area (Wangen et al., 2015). Glacial loading might have caused a significant increase of fluid pressure in the De Geerdalen Fm reservoir, which was enough to overcome the mechanical strength of the caprock shale. Pressure-activated flow paths such as fractures or solitary porosity waves might have formed in response to fluid pressure increase (Connolly and Podladchikov, 2007; Raess et al., 2014; Rozhko et al., 2007; Yarushina et al., 2015) generating chimney-like features. These could serve as fast fluid flow pathways by temporarily increasing vertical permeability, and enhancing diffusion rates by decreasing tortuosity and retardation in the vertical direction. Such a mechanism could have enhanced shale properties sufficiently to be responsible for producing the fluid mixing relation in segment D on a reasonable timescale. As fluid escaped from overpressured reservoir and normal fluid pressure was restored, the pressure-

activated flow-paths would have closed again. Subsequent deglaciation would reduce fluid pressure in the reservoir even further and efficiently restore the sealing properties of the caprock. Ongoing diffusional mixing would then have smoothed out any irregularities with depth inherited from the transient fluid flow.

Communication between segments E and F

The largest step change in the formation water $^{87}Sr/^{86}Sr$ profile occurs within the De Geerdalen Fm between 815.2 m and 820.8 m depth (Fig. 3), defining the junction between segments E and F. Comparison with the detailed lithological description of the DH4 core in Braathen et al. (2012) indicates that this compositional break occurs across a package of mudstones of lagoonal origin. The change in formation water $^{87}Sr/^{86}Sr$ composition indicates that these lagoonal mudstones form a significant barrier to water mixing between segments E and F.

Diffusion modelling (using the equation provided in Appendix B) provides some constraints on the lateral extent of this barrier effect. If there was no barrier, there would not be a sharp step change in $^{87}Sr/^{86}Sr$ between segments E and F. Even with incomplete mixing the sharp step would start to evolve into an S-shaped profile after only a few million years (Fig. 8), and this is clearly not the case.

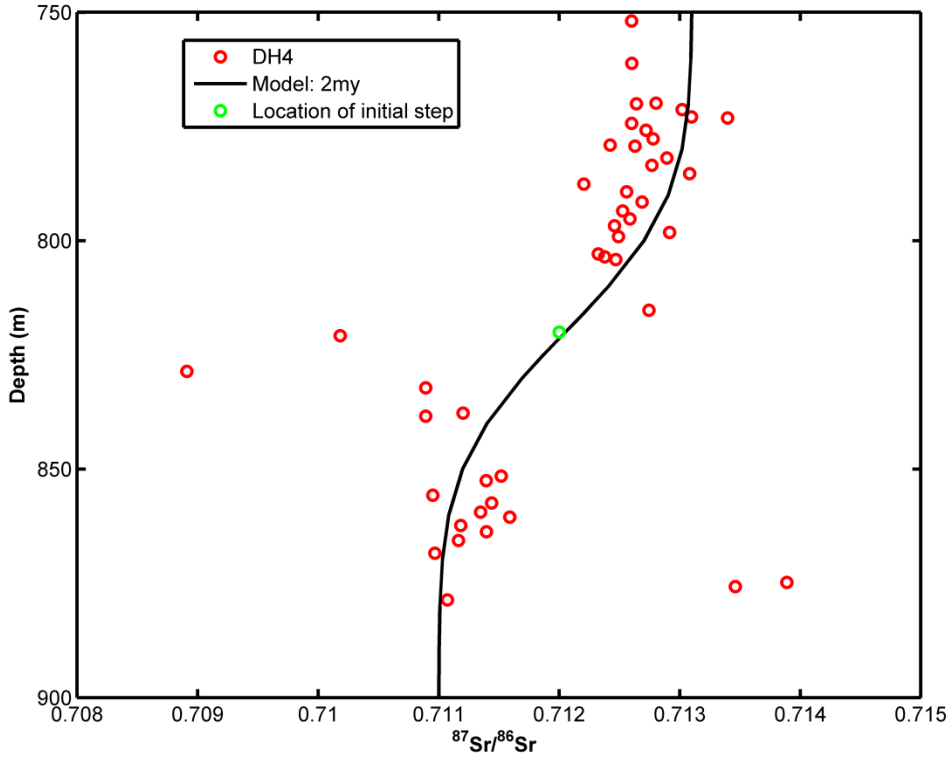

Fig. 8: Sr-RSA data for the De Geerdalen Fm in well DH4, showing step in composition at about 820 m depth. The curve is a diffusion mixing model for an initial sharp step at 820 m, after 2 my of mixing.

Mixing times to reach homogeneity can be approximated using the equation (Smalley et al., 1995):

$$t = 0.1\ L^2/D$$

where t and D are as defined previously, and L in this case is the radius of the barrier assuming the well to be at the centre of a circular barrier. Based on this, the $^{87}Sr/^{86}Sr$ measurements closest to the step change (at 815.2 m and 820.8 m, Fig. 8) would have mixed to the point of being indistinguishable from analytical uncertainty after only about 40,000 years if no barriers were present. The persistence of a sharp step is indicative of a barrier to mixing. To estimate the lateral extent of this barrier, the timescale for mixing must be assumed. For example, if 2 my was assumed, the

barrier length (i.e. diameter) would have to be greater than ~200 m to maintain the step change in water composition.

Additional constraints can be derived from the pressure data given by Braaten et al. (2012). This shows that, although segments E and F (Fig. 3) are both underpressured relative to a normal hydrostatic gradient, segment F is depleted by a further ~48 bar relative to segment E. The geometry of two bodies of sand separated by a shale barrier can be modelled using equation 19 in Muggeridge et al. (2004), explained in Appendix C. Assuming that the two measured pressures for segments E and F each apply to the whole thickness of the segment (150 m and 100 m respectively) the initial 48 bar pressure difference would homogenize within ~2000 years in the absence of any barrier. If, as above, the time available for mixing was assumed as 2 my, then a barrier of 1500 m diameter would be needed to maintain the observed pressure difference.

There is clearly uncertainty in this modelling due to the poor constraints on the assumption of available mixing time. However, the combination of step changes in both Sr isotope composition and pressure strongly indicate a significant barrier to vertical fluid mixing within the De Geerdalen reservoir interval. This could be significant for the planning the optimal depth for CO_2 injection, as injection below this barrier could reduce the risk of upward migration of the injected fluid (Ogata et al., 2012) and encourage its dispersion laterally (Woods, 2015).

5.2 Gas compositions and isotope analysis

The modelling (Appendix A) for correction of carbon isotopes for fractionation during degassing showed that the gas evolved at time step 1 was close to the modelled original bulk gas (within 5‰, usually within 2‰), much less than the dynamic range of

563 the gas dataset. Thus for methane and CO_2 it may be assumed that the gas from the
564 first time step is an acceptable proxy for the bulk CO_2 isotopic composition.

565 Similar to the Sr isotope data, the effect of gradual fluid mixing was also evident in
566 the core gas stable isotope data. The $\delta^{13}C$ values of methane show a gradual
567 upwards transition from typical thermogenic values at depth, towards lower values of
568 probable biogenic origin towards the top of the well. At the permafrost layer, the very
569 low methane $\delta^{13}C$ (<-65‰) indicates a biogenic microbial origin (e.g. Schoell, 1980;
570 Kotarba et al., 2013) of the degassed methane (Fig. 5). Above 200m in the upper
571 aquifer, methane $\delta^{13}C$ is -50 to -60‰ while CO_2 $\delta^{13}C$ reaches high values of >+10‰,
572 indicating microbial methanogenesis (Fig. 5) (e.g. Schoell, 1980; Kotarba et al.,
573 2013). This is also the section in which the gas is very dry, with the C1/(C2+C3) ratio
574 reaching close to 5000. The much higher concentration of methane relative to ethane
575 and propane (Fig. 3) supports methanogenesis as being dominant in this section.
576 The variable gas compositions and isotope ratios in this section indicate that the gas
577 compositions have not had time to equilibrate between the cap rock and the upper
578 aquifer.

579 The $\delta^{13}C$ of methane in the caprock is constant at about -50‰ from 200-300 m, and
580 then has a gradual depth-wise increase from -50 to -33‰ from 300 m down to 680 m.
581 In the latter section, there is no indication of biogenic gas from methane and CO_2
582 $\delta^{13}C$ data. The highly variable CH_4 concentrations in the extracted gas (Fig. 4) may
583 reflect extraction efficiency as well as the original gas content. Since we quantified
584 the possible isotope fractionation during the extraction process (Table A1; Appendix
585 A), and verified this to be small in this section (<2‰) compared to the variations with
586 depth (~33‰), the isotope data are interpreted to represent a real depth-wise

gradient. The gradual change in methane $\delta^{13}C$ with depth (Fig. 5) could be interpreted in three ways:

1. Local generation of methane from organic matter in the caprock shale, with the depth trend being caused by variation in source material or maturation. In this scenario, there would probably have been some limited vertical mixing of methane by diffusion to smooth out any local variations caused by variable source material
2. A model that has been invoked in other shales (Lu et al., 2015) is that the methane is not internally sourced within the shale, but migrates from the underlying reservoir upwards through the shale due to diffusion, with $\delta^{13}C_{methane}$ being fractionated by the diffusion process itself, due to differential retardation of ^{12}C and ^{13}C. We reject this model because the shape and direction of the $\delta^{13}C_{methane}$ curve is completely different to that expected from this process, as reported by Lu et al. (2015).
3. The caprock $\delta^{13}C_{methane}$ trend could be the result of internally –sourced methane as in model (1) gradually mixing by diffusion with isotopically heavier methane derived from the reservoir beneath.

Both scenarios 1 and 3 could apply, but scenario 1 involves a coincidental systematic change in organic matter isotopic composition with depth. Scenario 3 is thus preferred. Scenario 3 is amenable to diffusion modelling in the same way as was used for the Sr isotopes. However, there is much uncertainty in such modelling due to the lack of data on the sorption of dissolved methane and its effect on diffusion rates. We assume here a D_{eff} of 7.57×10^{-3} m^2y^{-1}, after the experimental results of Jacops et al. (2013), but there is considerable uncertainty about how representative their shale samples were to the caprock shale in the present study. The results of

612 diffusion modelling using the same equation as for Sr (Appendix B) but with the D_{eff}
613 cited above are shown in Figure 9.

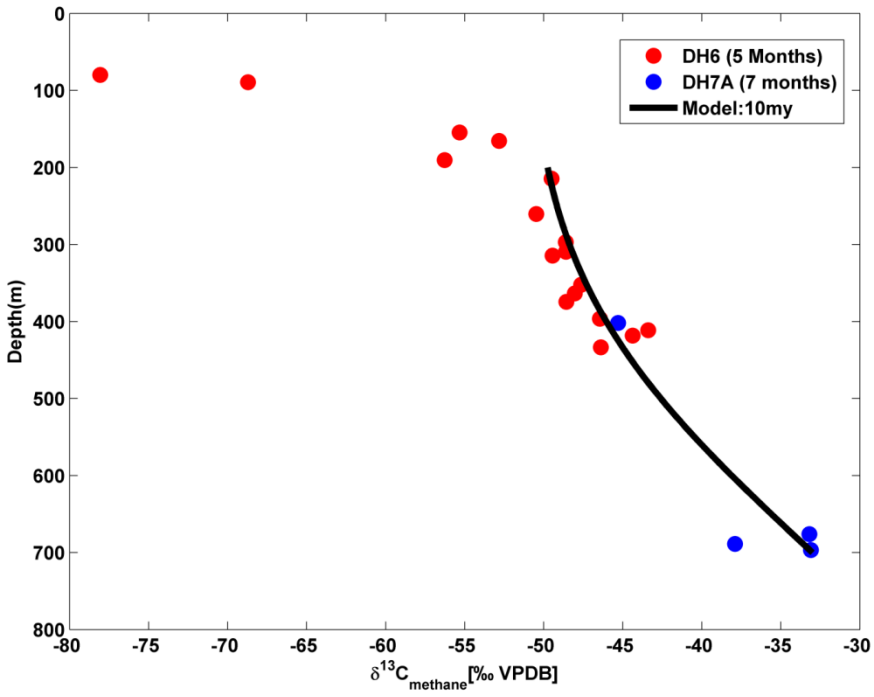

614

615 **Fig. 9:** Diffusion models for methane mixing with constant methane composition at
616 the base of the caprock shale.

617 Two cases were modelled, where the fixed isotopic composition of methane was at
618 the top and base of the caprock respectively. The sense of curve of the data
619 indicates that, as with Sr, the base of the caprock has a fixed composition. This
620 indicates that the underlying reservoir is the source of methane with a constant
621 isotopic composition (-33‰) that is gradually diffusing upwards through the caprock
622 shale and modifying its bulk composition. The modelled diffusion curve matches the
623 data with a timescale of 10 my (Fig. 9). In other words, the data fit with an influx of
624 isotopically heavier methane of dominantly thermogenic origin (Schoell, 1980;
625 Kortaba et al., 2013) at about 10 my ago. This is much shorter than the apparent
626 timescale for Sr diffusion through the caprock (Fig. 7) because methane diffuses
627 much more rapidly.

628 The CO_2 isotope data (Fig. 5) can be modelled in a similar manner (Fig. 10), although
629 depth-wise trends in the CO_2 data are less convincing than with methane.

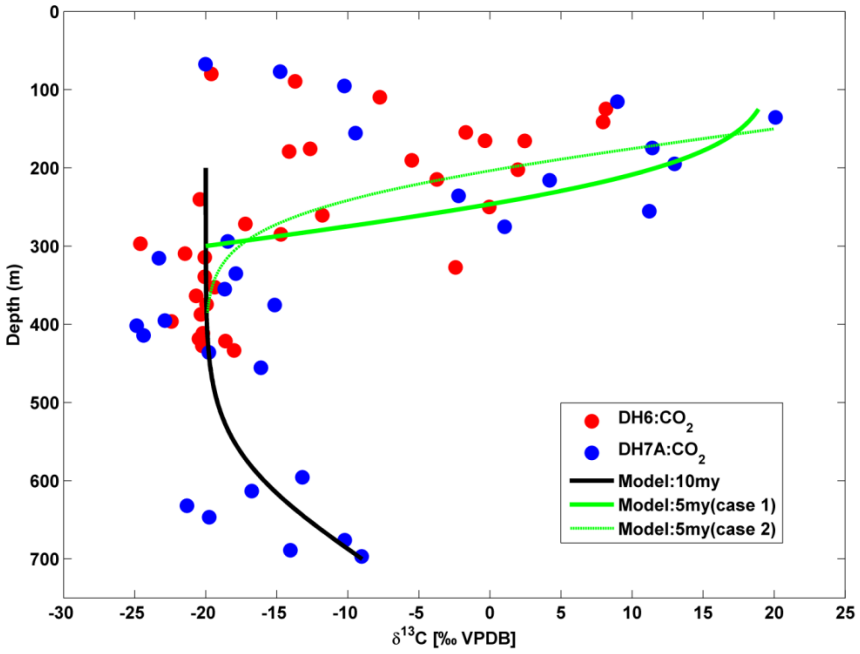

630

631 **Fig. 10:** Diffusion models for CO_2 mixing. The black curve is for caprock-reservoir
632 mixing with the underlying reservoir composition being constant. The green curves
633 are for aquifer-caprock mixing, with the thin line relating to the uppermost (aquifer)
634 composition being held constant, the bold green line to the lowermost value being
635 held constant.

636 In the caprock between about 300 m and 430 m depth, the $\delta^{13}C$ of CO_2 is relatively
637 constant at about -20‰. Below that, the $\delta^{13}C$ is rising to about -10‰ at the base of
638 the caprock close to the reservoir. This was modelled using the same equations as
639 for methane, but using a D_{eff} for CO_2 of 1.26 x 10^{-3} m^2y^{-1}, after Busch et al. (2008).
640 The caprock CO_2 data below 300m depth cannot be matched by models where the
641 caprock CO_2 $\delta^{13}C$ is constant, but resembles models where the underlying reservoir
642 CO_2 composition is constant, and the CO_2 diffuses upwards into the caprock,
643 gradually increasing its $\delta^{13}C$ (solid black curve on Fig. 10).

644 The model matches the CO_2 data with a mixing time of 10 my, as with methane (Fig
645 9), supporting the scenario of the reservoir becoming active as a supplier of methane
646 and CO_2 with a constant composition at about 10 my.

647 Towards the top of the caprock, the $\delta^{13}C$ of CO_2 increases towards the higher values
648 diagnostic of methanogenesis in the aquifer (+20‰, Fig. 10). A similar diffusion
649 model was applied also to this section. The noisiness of the $\delta^{13}C$ data makes it
650 difficult to determine which model is the better fit. However, the lack of a clear break
651 in composition at 300 m is an argument in favour of the upper (aquifer) end of the
652 mixing curve being constant (thin green curve on Fig. 10), with a mixing time of ~5
653 my. The favoured interpretation is thus that methanogenesis in the aquifer began
654 around 5 my ago, and the isotopically heavy CO_2 has since been diffusing
655 downwards into the upper part of the caprock.

656 The methane and CO_2 isotope data thus suggest that, although there is vertical
657 mixing of gases over a period of 5-10 my, gas movement within the caprock section
658 is slow, much slower than the timescale relevant for a CCS project. The overall
659 variations in gas $\delta^{13}C$ values indicate different processes controlling methane origins
660 in the permafrost, aquifer, upper and lower caprock and reservoir sections, and
661 indicate only very slow vertical communication of dissolved gases through the
662 sequence.

663 ## 6 Conclusions

664 This paper shows how oil and gas industry techniques for assessing reservoir
665 compartmentalization may also be useful for investigating prospective CO_2 storage
666 sites, helping to constrain material parameters and the past history of fluid
667 communication in the reservoir and caprock. The major conclusions are:

- $^{87}Sr/^{86}Sr$ of Sr dissolved in formation water, sampled using residual salt analysis, and gas isotope geochemistry are effective tools to understand the fluid communication in reservoirs and caprock shale on a geological timescale, and thus to help constrain the long-term behaviour of a potential CO_2 storage site.
- At the Longyearbyen site, systematic variations of the $^{87}Sr/^{86}Sr$ in formation water and the $\delta^{13}C$ of methane and CO_2 with depth in the caprock shale are consistent with slow diffusive mixing of these species over millions of years. This is a positive factor for the caprock acting as an effective barrier within the shorter time scale of potential CCS operations.
- However, the isotope data can only be explained if the vertical diffusivity and/or permeability have been accelerated at some time in the past. This could be related to transient changes in rock properties during deep burial and uplift, or glacial loading and unloading.
- The identified presence of a lagoonal mudstone barrier within the reservoir could form an additional barrier for the vertical flow of injected CO_2 and aid the dispersion of an injected CO_2 plume.

Acknowledgements

This work was supported in part by FME SUCCESS under grant 193825/S60 from Research Council of Norway, LYB De-risking project (Gassnova and UNIS CO_2 lab) and IFE's strategic funds. Fred Martin Kaaby and Christian Alexander Schoepke are thanked for their analysis on GC and GC-IRMS. The authors are thankful to Kjersti Iden for the XRD analysis. Harry Hjelmset is specially thanked for preparing and

692 measuring the samples for Sr RSA. Professor Ann Muggeridge (Imperial College) is
693 thanked for her guidance on diffusion modelling.

694

695 **References**

696 Anell, I., Braathen, A., and Olaussen, S. 2014. The Triassic – Early Jurassic of the
697 northern Barents Shelf: a regional understanding of the Longyearbyen CO_2
698 reservoir. Norwegian Journal of Geology, 94, 83–98.

699 Bachu, S., 2003. Screening and ranking of sedimentary basins for sequestration of
700 CO_2 in geological media in response to climate change. Environmental Geology,
701 44 (3), 277-289.

702 Bachu, S. and Adams, J.J., 2003. Sequestration of CO_2 in geological media in
703 response to climate change: capacity of deep saline aquifers to sequester CO_2
704 in solution. Energy Conversion and Management 44 (20), 3151-3175

705 Benson, S. M. and Cole, D. R. 2008. CO_2 Sequestration in Deep Sedimentary
706 Formations. Elements, 4, 325–331.

707 Berner, U., Faber, E. & Stahl, W. 1992. Mathematical simulation of the carbon
708 isotopic fractionation between huminitic coals and related methane. Chemical
709 Geology: Isotope Geoscience section 94, 315-319.

710 Bohloli, B., Skurtveit, E., Grande, L., Titlestad, G. O., Børresen, M. H., Johnsen, Ø.
711 and Braathen, A. 2014. Evaluation of reservoir and cap-rock integrity for the
712 Longyearbyen CO_2 storage pilot based on laboratory experiments and injection
713 tests. Norwegian Journal of Geology, 94, 171–187.

714 Braathen, A., Bælum, K., Christiansen, H. H., Dahl, T., Eiken, O., Elvebakk, H.,
715 Hansen, F., Hanssen, T. H., Jochmann, M., Johansen, T. A., Johnsen, H.,
716 Larsen, L., Lie, T., Mertes, J., Mørk, A., Mørk, M. B., Nemec, W., Olaussen, S.,
717 Oye, V., Rød, K., Titlestad, G. O., Tveranger, J. and Vagle, K. 2012. The
718 Longyearbyen CO_2 Lab of Svalbard, Norway-initial assessment of the geological
719 conditions for CO_2 sequestration. Norwegian Journal of Geology, 92, 353–376.

720 Buenz, S., Polyanov, S., Vadakkepuliyambatta, S., Consolaro, C., Mienert, J. 2012.
721 Active gas venting through hydrate-bearing sediments on the Vestnesa Ridge,
722 offshore W-Svalbard. Marine Geology 332–334, 189–197.

723 Busch, A., Alles, S., Gensterblum, Y., Prinz, D., Dewhurst, D.N., Raven, M.D.,
724 Stanjek, H. and Krooss, B.M. 2008. Carbon dioxide storage potential of shales.
725 International Journal of Greenhouse Gas Control 2, 297-308.

726 Connolly, J. A. D. and Podladchikov, Y. Y. 2007. Decompaction weakening and
727 channeling instability in ductile porous media: Implications for asthenospheric
728 melt segregation. Journal of Geophysical Research, 112, B10205.

729 Doughty, C., Freifeld, B. M., and Trautz, R. C. 2008. Site characterization for CO_2
730 geologic storage and vice versa: the Frio brine pilot, Texas, USA as a case
731 study. Environmental Geology, 54, 1635–1656.

732 Eberlei, T., Habler, G., Wegner. W., Schuster, R., Körner, W., Thöni, M. and Abart,
733 R., 2015. Rb/Sr isotopic and compositional retentivity of muscovite during
734 deformation. Lithos, 227, 161-178.

735 Fokker, P. A., Visser, K., Peters, E., Kunakbayeva, G., and Muntendam-Bos, A.G.
736 2012. Inversion of surface subsidence data to quantify reservoir
737 compartmentalization: A field study. Journal of Petroleum Science and
738 Engineering, 96–97,10–21.

739 Go, J., Bortone, I., Muggeridge, A.H., and Smalley, P.C. 2014. Predicting Vertical
740 Flow Barriers Using Tracer Diffusion in Partially Saturated, Layered Porous
741 Media. Transport in Porous Media, 105, 255-276.

742 Go, J., Smalley, P.C., and Muggeridge, A.H. 2012. Appraisal of reservoir
743 compartmentalization using fluid mixing time-scales: Horn Mountain Field, Gulf
744 of Mexico. Petroleum Geoscience, 18, 305-314

745 Harrington, J. F. Noy, D. J., Horseman, S. T., Birchall, D. J. and Chadwick, R. A.
746 2009. Laboratory Study of Gas and Water Flow in the Nordland Shale, Sleipner,
747 North Sea. Carbon dioxide sequestration in geological media—State of the
748 science: AAPG Studies in Geology 59, p. 521– 543.

749 Holloway, S., 1997. An overview of the underground disposal of carbon dioxide.
750 Energy Conversion and Management, 38, S193-S198.

751 IPCC, 2005. IPCC Special Report on Carbon Dioxide Capture and Storage, Prepared
752 by working group III of the Intergovernmental Panel on Climate Change. Metz,
753 B., O.Davidson, H. C. de Coninck, M. Loos, and L.A. Meyer (eds.). Cambridge
754 University Press, Cambridge, United Kingdom and New York, NY, USA, 442 pp.
755 www.ipcc.ch.

756 Jacops, E., Volckaert, G., Weetjens, E. and Govaert. J. 2013. Determination of gas
757 diffusion coefficients in saturated porous media: He and CH_4 diffusion in Boom
758 Clay. Appl. Clay Sci., 83-84, 217-223.

759 Jolley, S. J., Fisher, Q. J., and Ainsworth, R. B. 2010. Reservoir
760 compartmentalization: an introduction. Geological Society, London, Special
761 Publications, 347, 1–8.

762 Jones, C. E. and Jenkyns, H. C. 2001. Seawater strontium isotopes, oceanic anoxic
763 events, and seafloor hydrothermal activity in the Jurassic and Cretaceous.
764 American Journal of Science, 301, 112–149.

765 Kotarba, M. J., Więcław, D., Dziadzio, P., Kowalski, A., Bilkiewicz, E., and
766 Kosakowski, P. 2013. Organic geochemical study of source rocks and natural
767 gas and their genetic correlation in the central part of the Polish Outer
768 Carpathians. Marine and Petroleum Geology, 45, 106-120.

769 Krupka. K.M., Kaplan, D.I, Whelan, G., Serne, R.J., and Mattigod, S.V. 1999.
770 Understanding variation in partition coefficient, Kd, values Volume II: Review of
771 Geochemistry and Available K_d Values for Cadmium, Cesium, Chromium, Lead,
772 Plutonium, Radon, Strontium, Thorium, Tritium (3H), and Uranium. United
773 States Environmental Protection Agency report EPA 402-R-99-004B.

774 Li, Y.H. and Gregory, S. 1974. Diffusion of ions in seawater and in deep-sea
775 sediments. Geochim. Cosmochim. Acta, 38, 703-714.

776 Lu, J., Larson, T.E. and Smyth, R.C. 2015. Carbon isotope effects of methane
777 transport through Anahuac shale – a core gas study. Journal of Geochemical
778 Exploration, 148, 138-149.

779 Magnabosco, C., Braathen, A, and Ogata, K. 2014. Permeability model of tight
780 reservoir sandstones combining core-plug and Miniperm analysis of drillcore;
781 Longyearbyen CO_2 Lab, Svalbard.

782 Mazurek, M,, Alt-Epping, P., Bath, A., Gimmi, T., Waber, H.N., Buschaert, S., De
783 Cannière, P., De Craen, M., Gautschi, A., Savoye, S.,, Vinsot, A., Wemaere, I.
784 and Wouters, L. 2011. Natural tracer profiles across argillaceous formations.
785 Applied Geochemistry, 26, 1035-1064.

786 McArthur, J. M., Howrath, R J., and Bailey, T. R. 2001. Strontium Isotope
787 Stratigraphy: LOWESS Version 3: Best Fit to the Marine Sr-Isotope Curve for 0–
788 509 Ma and Accompanying Look-up Table for Deriving Numerical Age. The
789 Journal of Geology, 109, 155–170.

790 Mearns, E. W. and McBride, J. J. 1999. Hydrocarbon filling history and reservoir
791 continuity of oil fields evaluated using $^{87}Sr/^{86}Sr$ isotope ratio variations in
792 formation water, with examples from the North Sea. Petroleum Geoscience, 5,
793 17–27.

794 Muggeridge, A.H., Abacioglu, Y., England, W.A., and Smalley, P.C. 2004. The
795 dissipation of anomalous pressures in the subsurface. Journal of Geophysical
796 Research 109, B11104, 1-16

797 Munz, I. A., Johansen, H., Huseby, O., Rein, E., and Scheire, O. 2010. Water
798 flooding of the Oseberg Øst oil field, Norwegian North Sea: Application of
799 formation water chemistry and isotopic composition for production monitoring.
800 Marine and Petroleum Geology, 27, 838–852.

801 Oldenburg, C. M. 2008. Screening and ranking framework for geologic CO_2 storage
802 site selection on the basis of health, safety, and environmental risk.
803 Environmental Geology, 54,1687–1694.

Ogata, K., Senger, K., Braathen, A., Tveranger, J. and Olaussen, S. 2012. The importance of natural fractures in a tight reservoir for potential CO_2 storage: a case study of the upper Triassic–middle Jurassic Kapp Toscana Group (Spitsbergen, Arctic Norway). Geological Society, London, Special publications, 374, http://dx.doi.org/10.1144/SP374.9

Plaza-Faverola, A., Bünz, S., and Mienert, J. 2011. Repeated fluid expulsion through sub-seabed chimneys offshore Norway in response to glacial cycles. Earth and Planetary Science Letters, 305, 297–308.

Räss, L., Yarushina, V. M., Simon, N. S. C., and Podladchikov, Y. Y. 2014. Chimneys, channels, pathway flow or water conducting features - an explanation from numerical modelling and implications for CO_2 storage. Energy Procedia 63, 3761 – 3774.

Ray, J.S. & Ramesh, R. 2000. Rayleigh fractionation of stable isotopes from a multicomponent source. Geochimica et Cosmochimica Acta 64, 299–306.

Roy, S., Senger, D., Braathen, A., Noormets, R., Hovland, M., Olaussen, S., 2014. Fluid migration pathways to seafloor seepage in inner Isfjorden and Adventfjorden, Svalbard. Norwegian Journal of Geology, 94, 99-119.

Rozhko, A. Y., Podladchikov, Y. Y. and Renard, F. 2007. Failure patterns caused by localized rise in pore-fluid overpressure and effective strength of rocks. Geophysical Research Letters, 34, L22304.

Sand, G., Braathen, A., & Olaussen, S. 2014. Longyearbyen CO_2 Lab - tales of research and education. Norwegian Journal of Geology 94, 77-82.

Schoell M. 1980. The hydrogen and carbon isotopic composition of methane from natural gases of various origins. Geochimica et Cosmochimica Acta, 44 (5), 649-661.

Schoell, M., Jenden, P.O., Beeunas, M.A., and Coleman, D.O. 1993. Isotope Analyses of Gases in Gas Field and Gas Storage Operations. Society of Petroleum Engineers, SPE Gas Technology Symposium, 28-30 June, Calgary, Alberta, Canada.

Shackley,S., Reiner, D., Upham, P., Coninck, H. de, Sigurthorsson, G., and Anderson, J. 2009. The acceptability of CO_2 capture and storage (CCS) in Europe: An assessment of the key determining factors Part 2. The social acceptability of CCS and the wider impacts and repercussions of its implementation. International journal of greenhouse gas control 3, 3 4 4 – 3 5 6.

Siebel, W., Reitter, E., Wenzel, T. and Blaha, U., 2005. Sr isotope systematics of K-feldspars in plutonic rocks revealed by the Rb–Sr microdrilling technique. Chemical Geology, 222, 183-199.

Shields, G. A. 2007. A normalised seawater strontium isotope curve: possible implications for Neoproterozoic-Cambrian weathering rates and the further oxygenation of the Earth. eEarth, 2, 35–42.

Smalley, P. C., and England, W. A., 1994. Reservoir compartmentalization assessed with fluid compositional data. Society of Petroleum Engineers, Reservoir Engineering, August 1994, 175-180.

Smalley, P.C., Higgins, A.C., Howarth, R.J., Nicholson, H., Jones, C.E., Swinburne, N.H.M. & Bessa, J. 1994. Seawater Sr isotope variations through time: A procedure for constructing a reference curve to date and correlate marine sedimentary rocks. Geology, 22, 431-434.

Smalley, P.C., Dodd, T.A., Stockden, I.L., Råheim, A., and Mearns, E.W. 1995. Compositional heterogeneities in oilfield formation waters: identifying them, using them. In: Cubitt, J.M. & England, W.A. (eds.), Reservoir Geochemistry. Geological Society Special Publication 86, 59-69.

Smalley, P.C., England, W.A., Muggeridge, A.H., Abacioglu, Y., and Cawley, S. 2004. Rates of reservoir fluid mixing: implications for interpretation of fluid data. In: Cubitt, J.M., England, W.A. & Larter, S. (Eds.), Understanding Petroleum Reservoirs: towards an Integrated Reservoir Engineering and Geochemical Approach. Geological Society, London, Special Publication 237, 99-113.

Strapoc, D., Schimmelmann, A., & Mastalerz, M. 2006. Carbon isotopic fractionation of CH_4 and CO_2 during canister desorption of coal. Organic Geochemistry 37, 152–164.

Verdon, J. P., Kendall, J. M., Stork, A. L., Chadwick, R. A., White, D. J. and Bissell, R. C. 2013. Comparison of geomechanical deformation induced by megatonne-scale CO_2 storage at Sleipner, Weyburn, and In Salah. Proceedings of the National Academy of Sciences 110, E2762-E2771.

Waldhober,M. de B., Daamen, D. and Faaij, A. 2009. Informed and uninformed public opinions on CO_2 capture and storage technologies in the Netherlands. International journal of greenhouse gas control 3, 3 2 2 – 3 3 2.

Wang, X., Li, X, Wang, C., Shi, B., Luo, C., Zhang, L., Lei, Y., Jiang, C. & Meng, Q. 2015. Carbon isotopic fractionation by desorption of shale gases. Marine and Petroleum Geology 60, 79-86.

Wangen, M., Souche, A., and Johansen, H. 2015. A model for underpressure development in a glacial valley, an example from Adventdalen, Svalbard. Basin Research, 1–18.

Woods, A.W. 2015. Flow in porous rocks: Energy and environmental applications. Cambridge University Press, 289pp.

Yarushina, V. M., Podladchikov, Y. Y., and Connolly, J. A. D. 2015. (De)compaction of porous viscoelastoplastic media: Solitary porosity waves. Journal of Geophysical Research, 120 (7), 4843–4862.

Appendix A. Carbon isotope fractionation data processing

The process for reconstructing the carbon isotope composition of the initial bulk methane gas contained in each core sample followed the steps shown in Figure A1.

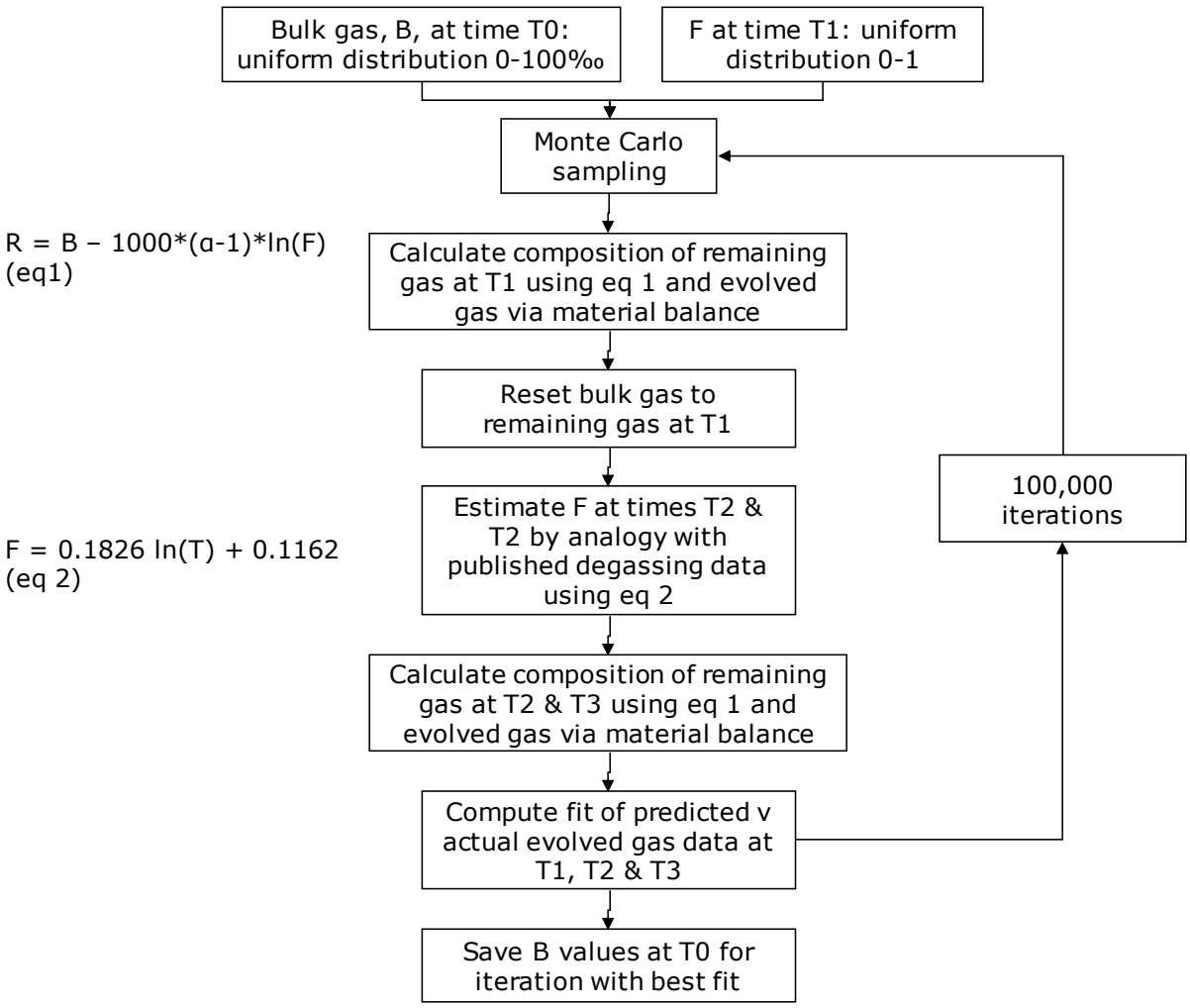

Fig. A1: Process for reconstructing carbon isotope compositions of bulk gases from core. B is the bulk methane $\delta^{13}C$ at time step T0 (prior to any degassing), which is unknown, and the objective of this process is to estimate this. Times T1, T2 and T3 are the three degassing sampling steps. F is the proportion of gas remaining in the sample (100% at T0). The equations are described in the text,

The relevant equation for the fractionation of gas isotopes during sample degassing can be written as:

$$R = B - 1000*(\alpha-1)*\ln(F) \quad (1)$$

where, R is the $\delta^{13}C$ of gas remaining in the sample, B is the bulk gas $\delta^{13}C$, F is the proportion of gas remaining in the sample and α is the fractionation factor. A factor of 1.003 was proposed for methane in coal samples by Berner et al. (1992). A trial of this equation using shale data from Wang et al. (2015) revealed a close fit to their data using α=1.003. In this study we thus used this same methane fractionation value.

The estimation of the initial bulk gas composition, B, from the degassed methane data is not trivial, because 1) the fraction evolved at each stage (F) is unknown, as pressures were not measured at each stage and 2) the methane was completely removed after the first sampling step, but gas was allowed to remain after subsequent steps, as described previously. To overcome these issues a Monte Carlo modelling method was used, as described below.

In Equation 1 there are two unknowns: the actual bulk methane composition (B), and the fraction (F) of gas remaining at each time of sampling. The bulk methane $\delta^{13}C$ was assigned a uniform probability distribution between 0 and -100‰ (most natural methane would fall within this range), while F at the time of first sampling (T1) was assigned a uniform probability distribution between and 0 and 1.00.

A Raleigh distillation model was constructed based on equation 1. For each sample where methane was sampled more than once, a Monte Carlo-style process was used to run the model 100,000 times and for each iteration, B at time T0 and F at first gas sampling (T1 = 5 or 7 months depending on the well) were sampled at random from the distributions described above. The model then assumed that the volume of gas evolved at T1 was lost, such that a new modified bulk composition for subsequent

time steps would be equal to R at T1. The $\delta^{13}C$ at subsequent sampling times was computed using equation 1 but with the modified B value (Figure A2).

The values of F at the times of subsequent sampling (T2,T3) were calculated by assuming that the shape of the desorption-time relation was similar to that of Strapoc et al. (2006), that can be approximated by a regression fit to their data:

$$1\text{-}F = 0.1826 \ln (T) + 0.1162 \quad (2)$$

Where 1-F is fraction of gas evolved and T is time in days.

The fraction desorbed at T1 (assigned a random value in step 1) was converted to time using equation 2, and then T2 and T3 times were scaled accordingly. For example where the fraction evolved (1-F) at T1 = 5 months (150 days) is 0.4, this equation gives time = 14.1 “days”. The timing of T2 and T3 at 12 and 26 months (365 and 780 days) would be re-scaled as 365*14.1/150 (34 “days”) and 780*14.1/150 (73 “days”) respectively. The rescaled T2 and T3 times were then substituted into the above equation to calculate F at T2 and T3.

For each of the 100,000 model iterations the calculated F and measured $\delta^{13}C$ values were compared with the $\delta^{13}C$ values predicted using equation 1, and quality of fit was calculated as $\sum(\text{predicted-measured})^2$ for the $\delta^{13}C$ values at T1 and T2 or T3. The iteration with the best quality of fit was retained. Repeat runs for each sample showed a variation at the <1‰ level in the calculated bulk $\delta^{13}C$ values.

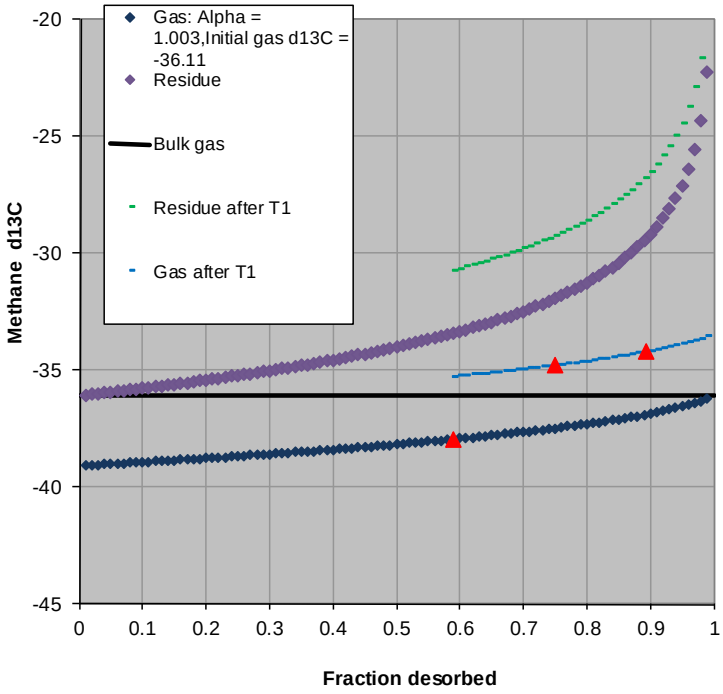

938

939 **Fig. A2**: Illustration of modelling process using sample DH7 688.89m. The curves are
940 best fits to the data (red triangles). The gas at T1 is fitted to an initial bulk gas
941 fractionation curve; the latter two samples are fitted to a modified curve rebased to a
942 new bulk composition after the gas at T1 has been removed. In this example, the
943 data are consistent with an initial bulk composition of -36.1‰.

944

945

946

947

948

949

950

951 **Table A1:** Carbon isotopes of methane degassed from core from wells DH6 and

952 DH7A at different sampling times, and modelled bulk methane carbon isotopes.

Well DH6							
			$\delta^{13}C_{Methane}$		$\delta^{13}C_{Methane}$	Fit	1-F
Lith	**Depth** (m)	**5 months** (‰ VPDB)	**12 months** (‰ VPDB)	**26 months** (‰ VPDB)	**Bulk** (‰ VPDB)		
PF	79.90	-78.071		-68.900	-74.3	8.825	0.31
PF	89.30	-68.715		-66.500	-66.4	0.003	0.61
Sst	154.54	-55.325	-49.400		-52.9	1.700	0.31
Sst	165.58	-52.825	-42.700		-48.2	18.207	0.31
Sst	190.31	-56.277	-48.000		-52.6	8.768	0.31
Sh	214.67	-49.501		-46.100	-47.5	0.003	0.45
Sh	260.49	-50.481		-48.700	-48.0	0.001	0.7
Sh	296.90	-48.614		-44.900	-46.7	0.002	0.41
Sh	309.58	-48.592		-43.200	-46.8	0.088	0.31
Sh	314.42	-49.443		-46.100	-47.6	0.006	0.44
Sh	352.42	-47.643	-42.452	-42.500	-46.0	0.014	0.31
Sh	363.55	-48.037		-43.300	-46.5	0.003	0.32
Sh	374.42	-48.568		-44.400	-46.9	0.007	0.36
Sh	396.42	-46.445	-43.216		-44.6	0.000	0.4
Sh	411.42	-43.394	-40.760		-41.4	0.002	0.47
Sh	418.43	-44.374		-39.100	-42.6	0.044	0.31
Sh	433.43	-46.394		-43.000	-44.4	0.001	0.45

Well DH7							
			$\delta^{13}C_{Methane}$		$\delta^{13}C_{Methane}$	Fit	1-F
Lith	**Depth** (m)	**7 months** (‰ VPDB)	**16 months** (‰ VPDB)	**28 months** (‰ VPDB)	**Bulk** (‰ VPDB)		
Sh	401.840	-45.3	-41.7	-38.5	-42.6	2.562	0.310
Sst	676.100	-33.2		-29.7	-31.4	0.005	0.400
Sst	688.890	-37.9	-35.6	-34.2	-36.1	0.000	0.390
Sst	696.820	-33.1		-28.0	-31.2	0.130	0.310

953

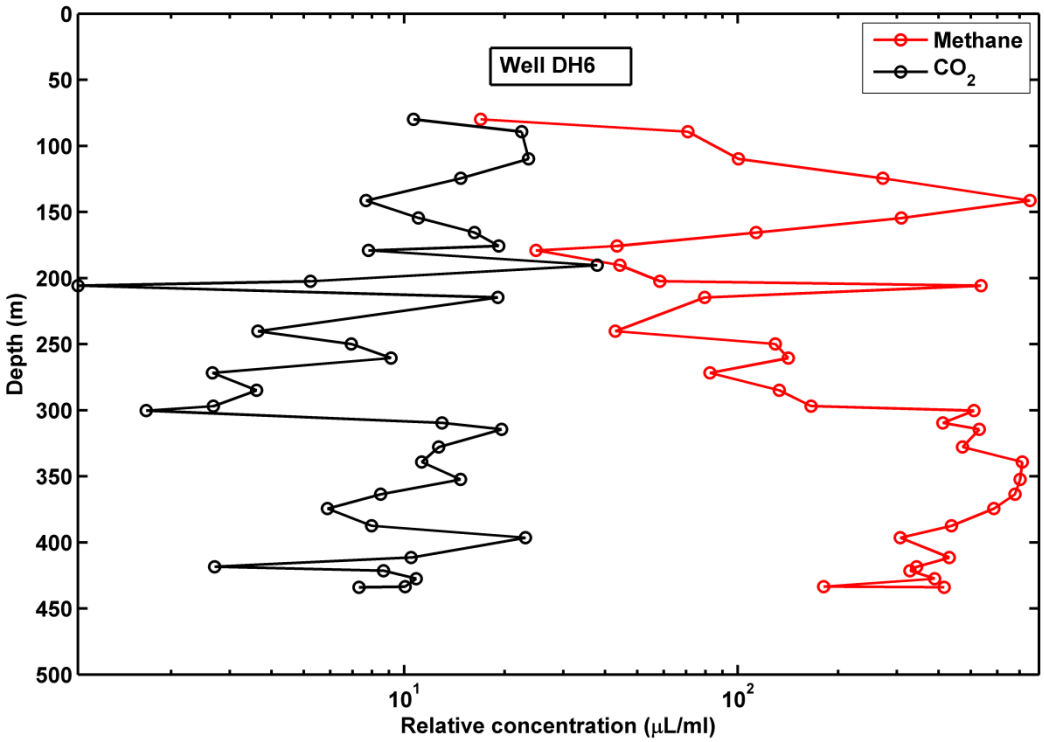

954

955 **Fig. A3:** Methane and CO_2 contents of gas degassed from well DH6 cores after five
956 months.

957 **Appendix B. Sr isotope mixing modelling**

958 When modelling the generation of the incomplete (i.e. non-steady-state) mixing
959 curves represented by segments B and D (Fig.3), there are two limiting cases that
960 can be considered:

961 (1) Solutes in two bodies of formation water are mixing, and both end-members are
962 of roughly similar size. In this case, both end-members will evolve in composition
963 through time, and the end steady state will be the whole system reaching a $^{87}Sr/^{86}Sr$
964 value of the size-weighted mean of the two end members. This style of mixing would
965 create an S-shaped mixing pattern with depth (cf. Fig. 8) that does not agree with the
966 shapes of segments B and D (Fig. 3).

967 (2) As above, but one of the mixing end-members has a fixed $^{87}Sr/^{86}Sr$ composition
968 – for example where one end member is a very much larger repository of Sr then the

other end member. In this case, the end steady state would be where the whole system attains the $^{87}Sr/^{86}Sr$ value of the dominant end member. This process is modelled as described below.

Mixing of Sr from two sources with one fixed end member can be described using the equation

$$C(x,t) = \frac{1}{2}\mathrm{erf}\left(\frac{x}{\sqrt{2Dt}}\right) + \frac{1}{2}$$

where C (x,t) is the concentration (or in this case the $^{87}Sr/^{86}Sr$ ratio, making the simplified assumption that Sr concentration does not vary) at a position x meters from the dominant end member at time t; and D is the effective diffusion coefficient for Sr. D is calculated following the method of Smalley et al. (1995, 2004) using the equation:

$$D = D_m \tau / R$$

Where D_m is the molecular diffusion coefficient for Sr, here with a value of 1.97x10-2 m^2y^{-1}, which is based on the value of Li and Gregory (1974) corrected to a temperature of 15°C; τ is the tortuosity of the rock, assumed to be 0.5, which is generous for these rather shaley rocks, and R is a retardation factor due to sorption of Sr onto the rock matrix. R is calculated as:

$$R = (1 + (1-\phi)\rho K)/\phi$$

Where ∅ is porosity (here approximated to an average value of 0.15, ρ is the density of the rock (estimated at 2650 kgm^{-3}), and K is the sorption distribution coefficient for Sr, here estimated at 0.005 m^3kg^{-1} (Krupka et al., 1999), based on groundwater in sediments with clay content >10%. Note that this is conservative; very sorptive

991 shales such as bentonites could have K values that are 2-3 orders of magnitude
992 greater.

993 Segment D was investigated using two cases, one where the segment C composition
994 was fixed, and segment E was variable, the other was vice versa. The “segment E
995 fixed” case fits the data very closely and is thus reported in Fig. 7, while the “segment
996 C fixed” case generated convex upward curves unlike the observed data.

997 The mixing of Sr isotope between segments E and F was modelled using a slightly
998 modified version of the mixing equation above, to allow intermixing of two variable
999 endmembers:

$$C(x,t) = \frac{c1 + c2}{2} - \frac{c1 + c2}{2}\mathrm{erf}\left(\frac{x}{\sqrt{2Dt}}\right)$$

1000

1001 **Table B1:** $^{87}Sr/^{86}Sr$ ratio over depth from Sr Residual Salt Analysis for the wells DH2,
1002 DH4, DH6, DH7A and DH8

Well No.	Depth (m)	$^{87}Sr/^{86}Sr$	2 sigma SD
DH2	762.57	0.713527	0.000019
DH2	766.42	0.713481	0.000013
DH2	771.79	0.715449	0.000017
DH2	779.83	0.714502	0.000014
DH2	780.36	0.713472	0.000012
DH2	786.22	0.714106	0.000018
DH2	796.85	0.713128	0.000021
DH2	807.14	0.713208	0.000026
DH2	817.94	0.713199	0.000014
DH2	821.79	0.713412	0.000011
DH2	828.24	0.713297	0.000012
DH2	835.65	0.713268	0.000016
DH2	840.93	0.713003	0.000011
DH2	844.43	0.712959	0.000012
DH2	849.61	0.712592	0.000016
DH2	850.85	0.712626	0.000017
DH4	85.32	0.708969	0.000019
DH4	105.11	0.711810	0.000020

DH4	125.22	0.711046	0.000018
DH4	145.10	0.716563	0.000022
DH4	165.35	0.717798	0.000017
DH4	185.34	0.717818	0.000016
DH4	210.30	0.718534	0.000022
DH4	260.55	0.720411	0.000022
DH4	310.33	0.720139	0.000024
DH4	461.87	0.718001	0.000021
DH4	509.21	0.717643	0.000020
DH4	553.87	0.716905	0.000017
DH4	665.32	0.712978	0.000017
DH4	669.30	0.713690	0.000030
DH4	671.60	0.713254	0.000022
DH4	675.50	0.713240	0.000020
DH4	676.40	0.713104	0.000017
DH4	678.10	0.713140	0.000016
DH4	680.50	0.713341	0.000015
DH4	681.90	0.713489	0.000019
DH4	687.30	0.713264	0.000018
DH4	687.50	0.713201	0.000029
DH4	688.30	0.713006	0.000017
DH4	691.60	0.713670	0.000014
DH4	692.50	0.713149	0.000022
DH4	693.80	0.713229	0.000023
DH4	695.40	0.712883	0.000022
DH4	698.50	0.713077	0.000018
DH4	702.80	0.712978	0.000024
DH4	703.70	0.712530	0.000019
DH4	705.80	0.713056	0.000024
DH4	708.80	0.712915	0.000013
DH4	712.80	0.713394	0.000016
DH4	715.60	0.713195	0.000020
DH4	718.40	0.712935	0.000022
DH4	721.50	0.712596	0.000019
DH4	727.30	0.713135	0.000017
DH4	737.34	0.713001	0.000016
DH4	746.83	0.712884	0.000011
DH4	751.90	0.7126	0.000015
DH4	761.14	0.712602	0.00001
DH4	769.90	0.712802	0.000018
DH4	770.00	0.71264	0.000013
DH4	771.30	0.713019	0.000020
DH4	772.90	0.713097	0.000032
DH4	773.10	0.713396	0.000015
DH4	774.30	0.712600	0.000013
DH4	775.80	0.712720	0.000021
DH4	777.70	0.712778	0.000016

DH4	779.05	0.712421	0.000015
DH4	779.30	0.712627	0.000021
DH4	781.90	0.712893	0.000017
DH4	783.50	0.712768	0.000022
DH4	785.30	0.713082	0.000016
DH4	787.60	0.712204	0.000018
DH4	789.30	0.712559	0.000039
DH4	791.50	0.712686	0.000014
DH4	793.50	0.712526	0.000017
DH4	795.20	0.712587	0.000019
DH4	796.70	0.712458	0.000014
DH4	798.20	0.712915	0.000018
DH4	799.10	0.712491	0.000012
DH4	802.90	0.712323	0.000022
DH4	803.50	0.712377	0.000013
DH4	804.10	0.712468	0.000015
DH4	815.20	0.712743	0.000018
DH4	820.80	0.710182	0.000018
DH4	828.60	0.708909	0.000019
DH4	832.20	0.710891	0.000016
DH4	837.70	0.711201	0.000038
DH4	838.40	0.710891	0.000039
DH4	851.50	0.711519	0.000014
DH4	852.50	0.711393	0.000029
DH4	855.70	0.710951	0.000012
DH4	857.40	0.711439	0.000026
DH4	859.40	0.711346	0.000014
DH4	860.50	0.711589	0.000009
DH4	862.30	0.711182	0.000024
DH4	863.70	0.711395	0.000046
DH4	865.60	0.711163	0.000033
DH4	868.40	0.710967	0.000030
DH4	874.80	0.713888	0.000072
DH4	875.70	0.713460	0.000021
DH4	878.60	0.711071	0.000032
DH4	887.70	0.711204	0.000021
DH4	896.90	0.711075	0.000018
DH4	897.40	0.710975	0.000023
DH4	898.70	0.711028	0.000023
DH4	899.20	0.710937	0.000018
DH4	901.50	0.710838	0.000027
DH4	902.50	0.711145	0.000016
DH4	969.60	0.711554	0.000044
DH6	109.65	0.709692	0.000015
DH6	141.25	0.715182	0.000017
DH6	175.56	0.716267	0.000013
DH6	179.00	0.715769	0.000022

DH6	190.40	0.717037	0.000019
DH6	202.28	0.720042	0.000014
DH6	240.14	0.720678	0.000015
DH6	244.38	0.719345	0.000013
DH6	249.84	0.720335	0.000017
DH6	271.68	0.720479	0.000017
DH6	284.85	0.720581	0.000018
DH6	300.15	0.720038	0.000015
DH6	326.85	0.720163	0.000016
DH6	339.18	0.719926	0.000019
DH6	363.13	0.719404	0.000026
DH6	387.00	0.719287	0.000019
DH6	400.50	0.719012	0.000011
DH6	407.70	0.719089	0.000023
DH6	421.00	0.718984	0.000019
DH6	427.00	0.718896	0.000027
DH7	67.34	0.710155	0.000017
DH7	76.72	0.709811	0.000015
DH7A	95.01	0.709696	0.000012
DH7A	115.25	0.709918	0.000017
DH7A	135.42	0.711610	0.000014
DH7A	155.49	0.715095	0.000015
DH7A	174.47	0.718048	0.000047
DH7A	175.00	0.717271	0.000015
DH7A	194.84	0.718999	0.000015
DH7A	215.73	0.720044	0.000013
DH7A	235.68	0.720157	0.000012
DH7A	255.29	0.720265	0.000016
DH7A	275.21	0.720579	0.000013
DH7A	294.00	0.720566	0.000018
DH7A	315.42	0.71937	0.00002
DH7A	335.00	0.719928	0.000022
DH7A	355.00	0.719222	0.00002
DH7A	375.25	0.719464	0.000016
DH7A	414.00	0.719456	0.000019
DH7A	455.43	0.718471	0.000011
DH7A	613.00	0.716197	0.000024
DH7A	646.50	0.714035	0.000015
DH8	31.45	0.710518	0.000015
DH8	43.00	0.709982	0.00002

1003

1004

1005

Table B2: $^{87}Sr/^{86}Sr$ of Calcite at De Geerdalen Fm.

Depth (m)	Formation	Estimated amount	$^{87}Sr/^{86}Sr$	2 sigma SD
771.3	De Geerdalen	20 %	0.710396	0.000015
779.3	De Geerdalen	10 %	0.711280	0.000012
787.6	De Geerdalen	60 %	0.709585	0.000012
796.7	De Geerdalen	10 %	0.711167	0.000012
803.5	De Geerdalen	10 %	0.711160	0.000016
820.8	De Geerdalen	80 %	0.708731	0.000012
828.6	De Geerdalen	80 %	0.708297	0.000012
832.2	De Geerdalen	70 %	0.709505	0.000010
837.7	De Geerdalen	40 %	0.709912	0.000012
855.7	De Geerdalen	10 %	0.710130	0.000011
875.7	De Geerdalen	10 %	0.710592	0.000010

Appendix C. Pressure mixing between segments E and F.

The difference in pressures between segments E and F (Fig. 3) was interpreted by calculating how long it would take for the pressure to equilibrate in the presence of an intervening flow barrier with different lengths. The analytical expression used was that of Muggeridge et al. (2004):

$$t = -\frac{1}{\alpha^2}\frac{L^2 c\phi\mu}{4k} ln\left[\frac{\delta P}{\Delta P}\frac{R(R+1)+\alpha^2}{2R\ sec\ \alpha}\right]$$

Where t is the time to reach steady state (s), L is reservoir length (m), c is effective compressibility (Pa^{-1}), ϕ is porosity, μ is viscosity (Nsm^{-2}), k is permeability (m^2), δP is the pressure measurement resolution, ΔP is the initial pressure difference; R is $k_b L_b / 2kH_b$, where k_b is the barrier permeability, L_b is the barrier length, H_b is the barrier thickness; and where α is the first root of the transcendental function $\alpha \tan \alpha = R$.